COMMUNICATION

Self-polymerization of carbonyl pigments for high-performance aqueous ammonium-ion batteries†

Jinyao Yang,‡[a] Wendi Wang,‡[b] Zeyu Cao,[a] Jingyuan Zhang,[a] Hang Ren,[a] Ying Yang,[a] Huaiyu Shao [ID][c] and Shengyang Dong [ID] *[ac]

A self-polymerized carbonyl pigment, perylene-3,4,9,10-tetracarbo-xylic dianhydride (P420), is prepared by one-step heat treatment. Benefiting from molecular self-polymerization, the P420 electrode delivers a reversible capacity of 98.8 mA h g^{-1} at 0.1 A g^{-1} for aqueous ammonium-ion storage. Even at 5 A g^{-1}, 95 mA h g^{-1} can be retained.

Aqueous rechargeable batteries are increasingly attracting interest in the domain of sustainable energy storage research, mainly because of their affordability and nonflammable characteristics. Generally, energy storage systems employ metal ions like Li$^+$, Na$^+$, K$^+$, Mg^{2+}, Zn^{2+}, and Al^{3+} as charge carriers.[1–6] Nevertheless, nonmetallic ions, such as NH$_4^+$, feature a unique structure that has often been neglected. NH$_4^+$ presents multiple benefits, including low cost, widespread availability, small hydrated ionic size of 3.31 Å, and low molar mass of 18 g mol^{-1}, which promotes swift diffusion in aqueous environments.[7] Additionally, NH$_4^+$ does not generate dendrites, and the water-based electrolyte is less corrosive, which enhances safety. Consequently, it is well-suited for emerging industries, such as flexible wearable devices and standby energy storage systems.[8]

Recently, various transition metal materials, including VO$_2$,[9,10] MoO$_3$,[8] WO$_3$[11,12] and MoS$_2$,[13] have been utilized as negative electrodes in aqueous ammonium-ion batteries (AAIBs) to achieve high capacity and cycling stability. However, these transition metal-based electrode materials inevitably experience capacity attenuation due to structural degradation and the dissolution of active ions.[14] In contrast, organic materials present several advantages, including cost-effectiveness environmental sustainability, structural flexibility, and a wealth of oxidation-active sites.[15,16] Moreover, the flexible nature of organic structures, which diverges from the inflexible lattice of transition metals, facilitates the rapid embedding and extraction of NH$_4^+$, thereby enhancing high-rate performance.[17]

Ji's group reported that PTCDA serves as an anode, reaching an impressive specific capacity of 92 mA h g^{-1} at a current density of 0.24 A g^{-1}, with a coulombic efficiency of approximately 95%.[7] Cao *et al.* developed a polymer material (PNNI) for AAIBs, demonstrating a capacity retention of 80.2% over 10 000 cycles at 5 A g^{-1}, indicating impressive longevity in cycling performance.[15] Nevertheless, these materials exhibit poor electrical conductivity and high solubility in the electrolyte, which results in weak rate capacity and inadequate cycling stability. Previous reports have indicated that the thermal polymerization of PTCDA molecules can enhance their structure stability,[18] effectively addressing dissolution issues and improving electrode conductivity.[19] This underscores the significant potential of organic molecular polymerization for application in electrode materials.

In this work, we employed a one-step heat treatment to polymerize PTCDA molecules, resulting in the formation of P420, which serves as the anode material for AAIBs. This heat treatment not only increased the structure stability but also enhanced the activity of the C=O bonds within the PTCDA molecules. Consequently, the P420 electrode exhibits a reversible capacity of 98.8 mA h g^{-1} at 0.1 A g^{-1}. Additionally, a high-performance NH$_4^+$-based full cell, constructed with the P420 anode and copper hexacyanoferrate (Cu-HCF) cathode, demonstrates exceptional long-term cycling stability with a capacity retention of 96.9% over 800 cycles. This strategy of molecular thermal polymerization enhances the redox active sites, thereby improving electrochemical performance.

As illustrated in Fig. 1, the process of heat treatment aids in breaking the ester bond in the acyl anhydride group, which results in the creation of an oxyanion. To maintain the electroneutrality of the entire molecule, the negatively charged oxygen then proceeds to attack the carbon atom of the carbonyl group, thereby causing a coordination reaction.[18]
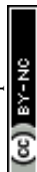
[a] *School of Chemistry and Materials Science, Nanjing University of Information Science and Technology, Nanjing 210044, China*

[b] *ZIBO XINCAIIC CO., LTD, Zibo 255000, China*

[c] *Institute of Applied Physics and Materials Engineering, University of Macau, Macau 999078, China*

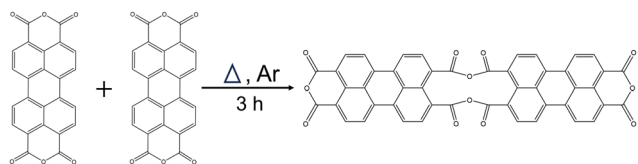‡ J. Yang and W. Wang are co-first authors.

Fig. 1   The polymerization reaction schematic diagram of PTCDA.

The thermogravimetric analysis (TGA) of PTCDA was conducted to study the heat treatment process (refer to Fig. S1, ESI†), with the temperature ranging from 30 °C to 700 °C. The results from TGA, combined with data from differential scanning calorimetry (DSC), indicate that polymerization began gradually after reaching 150 °C and stabilized at around 420 °C. A significant mass loss of PTCDA was notably recorded at temperatures exceeding 500 °C, suggesting considerable damage to its molecular framework. Thus, the equilibrium temperature determined by DSC at 420 °C, characterized by only slight mass loss, was established as a suitable annealing temperature to limit extensive decomposition of PTCDA. Moreover, control temperatures of 300 °C (referred to as P300) before reaching equilibrium, and 500 °C (designated as P500) after equilibrium, were selected (Fig. S1, ESI†). Fig. 2(a) exhibits the X-ray diffraction (XRD) patterns for both pristine PTCDA and P420 with a diffraction angle range from 5° to 35°. To improve the clarity of the characteristic peaks, expanded representations of the Bragg peaks (011), (002), (012), (11−1), and (10−3) are provided in Fig. 2(b) and Fig. S2 (ESI†). The XRD data indicate a slight enlargement of the interlayer spacing of the (011) plane post-annealing, as demonstrated by the peak shift in XRD from 9.0° to 8.9° (Fig. 2(b)). Furthermore, Fig. S3(a)–(c) (ESI†) illustrates the XRD patterns of P300 and P500, clearly demonstrating that the maximum offset occurs at 420 °C. These findings suggest that thermal polymerization is optimized at the equilibrium temperature identified through DSC.

In Fig. S4(a) (ESI†), α-PTCDA arranges itself into a columnar structure, where the long axis of the molecules within the central stack is oriented nearly perpendicular to the short axis of those in neighboring stacks. At the rectangular top corners of the columnar configuration, each atom is situated directly above its corresponding atom in the molecule beneath, leading to an exceptionally close inter-molecular distance of approximately 3.70 Å (Fig. S4(b), ESI†). Given the structural characteristics of PTCDA and the variation in crystal face spacing, this arrangement may facilitate the rapid transport of NH_4^+. As shown in Fig. 2(c), the scanning electron microscopy (SEM) image of pristine PTCDA reveals a homogeneous elongated microrod. Following annealing treatment, as illustrated in Fig. 2(d) and Fig. S5 (ESI†), the particle size increases compared to that of pristine PTCDA. These observations suggest that the heat treatment does not alter the morphology of pristine PTCDA, while the expansion of the rods reflects a macroscopic sign of increased layer spacing.

To investigate potential changes in the structure of the functional groups of heat-treated PTCDA organic molecules, infrared characterization tests were conducted. As illustrated in Fig. 3(a), the position of the C=O bond in P420 is significantly shifted compared to that in PTCDA, and the peak shape is sharper, indicating that hot polymerization enhances the activity of the C=O bond. Furthermore, the absorption peaks of the C=C bond and C–O–C bond exhibit reduced intensity, further corroborating the structural changes associated with the thermal polymerization of PTCDA. The same alterations can also be seen in P300 and P500 (Fig. S3(d), ESI†). Although characteristic peaks associated with C 1s (≈ 285 eV) and O 1s (≈ 533 eV) are observed in both materials, as illustrated in Fig. 3(b), high-resolution C 1s X-ray photoelectron spectroscopy (XPS) results (Fig. 3(c)) indicate a reduction in the peak intensity of C=O bonds (288.9 eV) alongside an increase in the intensity of C–O bonds, insinuating that the annealing process promotes the polymerization of PTCDA. Comparable trends are noted in the high-resolution O 1s XPS data (Fig. 3(d)), where pristine PTCDA reveals a greater proportion of C=O bonds in contrast to P420, while C–O bonds significantly
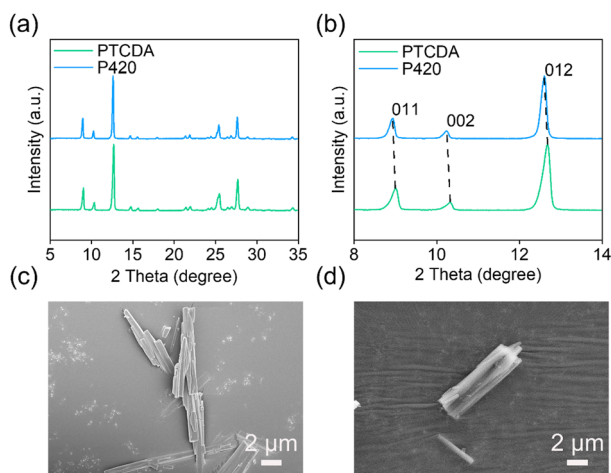

Fig. 2   (a) and (b) XRD patterns of pristine PTCDA and P420. SEM images of (c) pristine PTCDA and (d) P420.
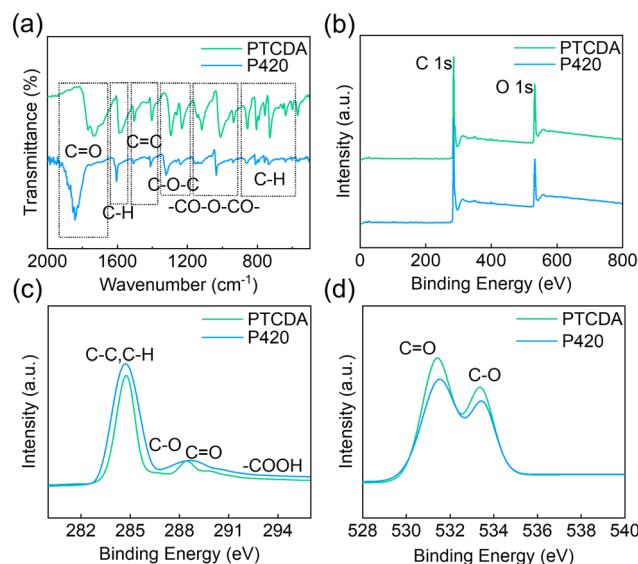

Fig. 3   Structure characterizations of pristine PTCDA and P420. (a) FTIR spectra. (b) Full XPS curves. (c) High-resolution C 1s XPS. (d) High-resolution O 1s XPS.

rise after annealing. Furthermore, following the annealing process, the binding energy of O 1s escalates, suggesting that the O atom enters an electron-deficient state, whereas the C atom adopts an electron-rich configuration. The presence of substantial aromatic carbon structures and characteristics of electron richness can notably accelerate the electron transport rate, potentially yielding highly conductive materials.

To investigate the electrochemical performance and assess the NH_4^+-storage kinetics of pristine PTCDA and P420, cyclic voltammetry (CV) and galvanostatic charge/discharge (GCD) tests were conducted within a potential range of -0.8 to 0.2 V (*vs.* Ag/AgCl) using a three-electrode setup. The CV curves for both pristine PTCDA and P420 exhibit a significant degree of overlap, indicating that thermal polymerization did not alter the NH_4^+ binding sites (Fig. S6, ESI†).

Furthermore, the galvanostatic charge–discharge curve corroborates the reversible redox process observed in the CV curves.

Additionally, the capacity of P420 is significantly higher than that of pristine PTCDA. For example, reversible capacities of 98.8 mA h g^{-1} and 77.3 mA h g^{-1} can be obtained, respectively, in the first cycle at 0.1 A g^{-1} (Fig. 4(a)). Benefiting from the self-polymerization reaction, the rate performance of P420 also surpasses that of pristine PTCDA; the average reversible specific capacities were recorded at 99.4, 98.7, 96.8, 95.5, 95.7, and 95 mA h g^{-1} for P420, in contrast to 76.4, 71.9, 70.5, 70.2, 70.6, and 70 mA h g^{-1} for pristine PTCDA at current densities of 0.1, 0.3, 0.5, 1, 3 and 5 A g^{-1}, respectively (Fig. 4(b)). As expected, the specific capacity of P420 exceeds that of pristine PTCDA. However, the electrochemical performance of P300 and P500 is significantly inferior to that of pristine PTCDA (Fig. S7(a)–(d), ESI†). The cycling stability of pristine PTCDA is inferior visibly, demonstrating considerable capacity fading (Fig. 4(c)). Although the specific capacity in P420 also decreased after 200 cycles, its capacity retention rate of 86% (81 mA h g^{-1}) was notably higher than the 72% (59 mA h g^{-1}) observed for pristine PTCDA. Furthermore, the galvanostatic intermittent

titration technique (GITT) was utilized to investigate the diffusion kinetics of NH_4^+ in both PTCDA and P420 (Fig. S8, ESI†). As shown in Fig. S8(a) and (b) (ESI†), the NH_4^+ diffusion coefficient (*D*) values during charge and discharge cycles were greater for P420 compared to PTCDA. Additionally, the advantages of heat treatment on PTCDA are evident in other metal ion batteries (Fig. S9, ESI†). Consequently, organic molecules effectively activate reactive sites through thermal self-polymerization, thereby enhancing capacity and cycling performance.

To investigate the charge storage mechanism of the P420 electrode in a 1 M $(NH_4)_2SO_4$ electrolyte, we gathered XRD and FT-IR data across various states of charge/discharge (SOCs, Fig. 5(a)). As illustrated in Fig. 5(b), no new characteristic peaks emerge during the charge–discharge process, with the exception of the unwashed $(NH_4)_2SO_4$ and Ti networks, indicating that no lattice phase transition occurs. Fig. 5(c) presents an enlarged view of the diffraction peaks corresponding to the (011) and (012) crystal faces. Notably, the (011) and (012) peaks shift to lower 2θ values from 8.9° and 12.6° (point I) to 8.7° and 12.4° (point III) during the discharge process. This shift suggests that the insertion of NH_4^+ results in an increase in the spacing of the P420 layers. Subsequently, during charging to 0.2 V, the (011) and (012) peaks gradually revert to their initial positions, demonstrating the good reversibility of the P420 lattice. *Ex situ* FT-IR assessments were performed to analyse the changes in functional groups within P420 (Fig. 5(d)). Notably, the characteristic peak at 1730 cm^{-1}, which corresponds to the stretching vibration of C=O, diminishes
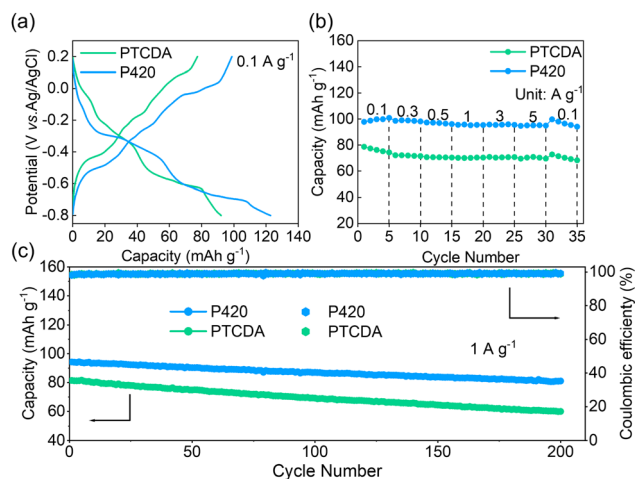

Fig. 4 Electrochemical performance of pristine PTCDA and P420. (a) Discharge/charge curves, (b) rate capability, and (c) cycling stability and coulombic efficiency.
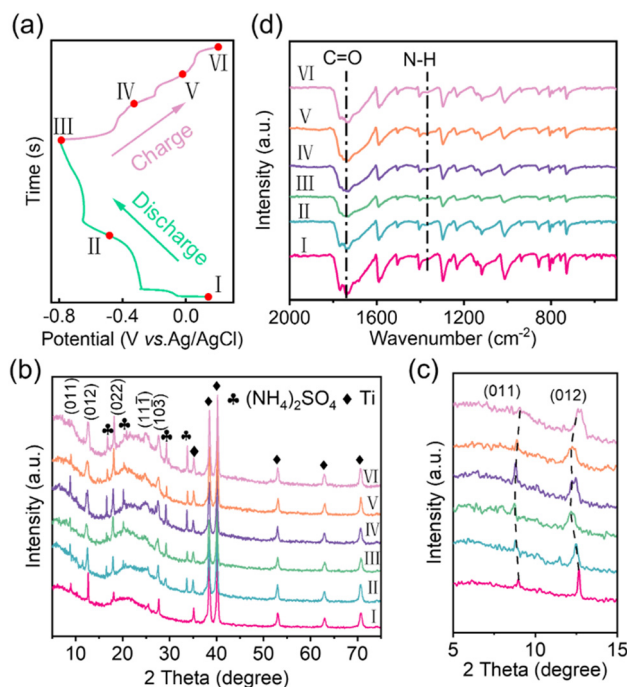

Fig. 5 (a) GCD curves of the P420 anode. Six SOCs were chosen. Point I: open-circuit potential state ($\sim$0.14 V), point II: discharge to −0.5 V, point III: discharge to −0.8 V, point IV: charge to −0.3 V, point V: charge to 0 V, and point VI: charge to 0.2 V. (b) XRD patterns under different SOCs. (c) Evolution of the (011) and (012) peaks.
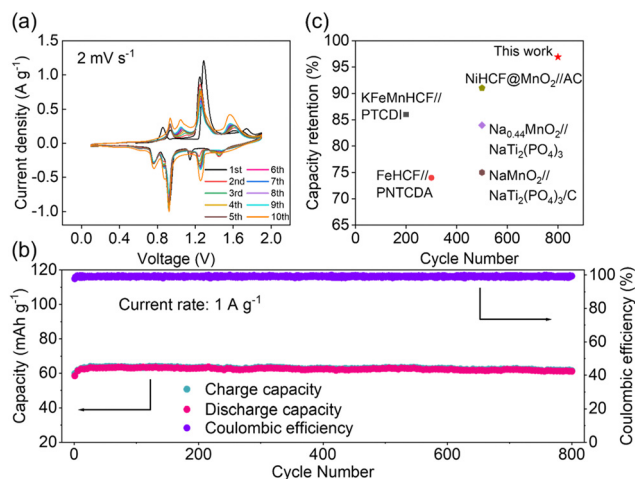
Fig. 6 Electrochemical performance of the Cu-HCF//P420 full cell. (a) Initial ten CV curves at 2 mV s^{-1}. (b) Cycling performance of the full cell at 1 A g^{-1}. (c) Capacity retention comparison graph.

progressively during the discharge phase, suggesting ongoing coordination of NH$_4^+$ with the carbonyl groups. In contrast, the subsequent variations in the C=O peak present a reverse trend. Furthermore, the absorption peak related to the N–H bond at 1365 cm^{-1} intensifies during discharge and gradually vanishes during the charging process, providing additional evidence of the high reversibility associated with the (de)insertion of NH$_4^+$. The proposed NH$_4^+$ incorporation mechanism is shown in Fig. S10 (ESI†).

We further fabricated a full cell using Cu-HCF as the cathode and P420 as the anode, adhering to a mass ratio of 2:1 in accordance with their discharge capacities. Comprehensive characterizations of the cathode material, encompassing structural and electrochemical performance results, are illustrated in Fig. S11, S12 and S13a (ESI†). The CV curves of the full cell, recorded at a scan rate of 2 mV s^{-1}, exhibit a strong overlap, indicating excellent reversibility, as shown in Fig. 6(a). Fig. S13(b) (ESI†) presents the GCD curve of the full cell at a current density of 0.1 A g^{-1}, demonstrating good repeatability and corresponding to the redox positions identified in the CV curve. To further assess the stability of the full cell, long-term cycling tests were conducted at a current density of 1 A g^{-1}. The AAIBs exhibited a capacity retention of approximately 96.9% of their maximum capacity after 800 cycles (Fig. 6(b)), which is comparatively superior for other reported aqueous batteries (Fig. 6(c)).[20–24]

In summary, we employed a one-step heat treatment to self-polymerize PTCDA molecules as an anode material for AAIBs. The molecular polymerization of PTCDA allows for the delocalization of electrons, significantly enhancing electron transport and cycling stability. Consequently, the P420 electrode exhibits a reversible specific capacity of 98.8 mA h g^{-1} at 0.1 A g^{-1}. Furthermore, a high-performance NH$_4^+$-based full cell, assembled with the P420 anode and Cu-HCF cathode, demonstrates remarkable long-term cycling stability, achieving 96.9% capacity retention over 800 cycles. This work introduces a novel

concept wherein organic molecules are thermally polymerized to enhance NH$_4^+$ storage performance, thereby promoting advancements in aqueous ammonium-ion batteries.

Data availability

The data supporting this article have been included as part of the ESI.†

Conflicts of interest

There are no conflicts to declare.

Notes and references

1 L. Zhang, X. Li, M. Yang and W. Chen, *Energy Storage Mater.*, 2021, **41**, 522–545.
2 M. Chen, L. Chen, Z. Hu, Q. Liu, B. Zhang, B. Hu, Q. Gu, J. L. Wang, L. Z. Wang, X. Guo, S. L. Chou and S. X. Dou, *Adv. Mater.*, 2017, **29**, 1605535.
3 J. Zhou, D. Shen, X. Yu and B. Lu, *J. Energy Chem.*, 2022, **69**, 100–107.
4 X. Shen, T. Sun, L. Yang, A. Krasnoslobodtsev, R. Sabirianov, M. Sealy, W. N. Mei, Z. Wu and L. Tan, *Nat. Commun.*, 2021, **12**, 820.
5 Q. Yang, F. Mo, Z. Liu, L. Ma, X. Li, D. Fang, S. Chen, S. Zhang and C. Zhi, *Adv. Mater.*, 2019, **31**, 1901521.
6 B. J. Kwon, L. Yin, H. Park, P. Parajuli, K. Kumar, S. Kim, M. Yang, M. Murphy, P. Zapol, C. Liao, T. T. Fister, R. F. Klie, J. Cabana, J. T. Vaughey, S. H. Lapidus and B. Key, *Chem. Mater.*, 2020, **32**, 6577–6587.
7 X. Wu, Y. Qi, J. J. Hong, Z. Li, A. S. Hernandez and X. Ji, *Angew. Chem., Int. Ed.*, 2017, **56**, 13026–13030.
8 G. Liang, Y. Wang, Z. Huang, F. Mo, X. Li, Q. Yang, D. Wang, H. Li, S. Chen and C. Zhi, *Adv. Mater.*, 2020, **32**, e1907802.
9 X. Mu, Y. Song, Z. Qin, J. Meng, Z. Wang and X.-X. Liu, *Chem. Eng. J.*, 2023, **453**, 139575.
10 Y. Wu, S. Dong, N. Lv, Z. Xu, R. Ren, G. Zhu, B. Huang, Y. Zhang and X. Dong, *Small*, 2022, **18**, e2204888.
11 X. Wen, J. Luo, K. Xiang, W. Zhou, C. Zhang and H. Chen, *Chem. Eng. J.*, 2023, **458**, 141381.
12 Y. Z. Zhang, J. Liang, Z. Huang, Q. Wang, G. Zhu, S. Dong, H. Liang and X. Dong, *Adv. Sci.*, 2022, **9**, e2105158.
13 X. Bai, Y. Jang, F. Zhang, Z. Jiang, F. Sun, H. Di, S. Ru, D. Liao and H. Zhang, *Dalton Trans.*, 2023, **52**, 4923–4932.
14 Z. Cao, J. Yang, H. Ren, J. Zhang, Y. Yang, G. Zhu, Y. Zhang and S. Dong, *Chem. Commun.*, 2024, **60**, 13911–13914.
15 S. Zhang, K. Zhu, Y. Gao and D. Cao, *ACS Energy Lett.*, 2023, **8**, 889–897.
16 Y. Ma, T. Sun, Q. Nian, S. Zheng, T. Ma, Q. Wang, H. Du and Z. Tao, *Nano Res.*, 2021, **15**, 2047–2051.
17 G. Zhou, X. An, C. Zhou, Y. Wu, Y.-E. Miao and T. Liu, *Compos. Commun.*, 2020, **22**, 100519.
18 Y. Liu, W. Luo, S. Lu, Z. Zhang, Z. Chao and J. Fan, *ACS Appl. Mater. Interfaces*, 2022, **14**, 53702–53710.
19 N. Liu, X. Wu, Y. Zhang, Y. Yin, C. Sun, Y. Mao, L. Fan and N. Zhang, *Adv. Sci.*, 2020, **7**, 2000146.
20 T. Hosaka, R. Takahashi, K. Kubota, R. Tatara, Y. Matsuda, K. Ida, K. Kuba and S. Komaba, *J. Power Sources*, 2022, **548**, 232096.
21 M. Wang, H. Wang, H. Zhang and X. Li, *J. Energy Chem.*, 2020, **48**, 14–20.
22 Y. Wang, L. Mu, J. Liu, Z. Yang, X. Yu, L. Gu, Y. S. Hu, H. Li, X. Q. Yang, L. Chen and X. Huang, *Adv. Energy Mater.*, 2015, **5**, 1501005.
23 Z. Hou, X. Li, J. Liang, Y. Zhu and Y. Qian, *J. Mater. Chem. A*, 2015, **3**, 1400–1404.
24 Y. Wang and Q. Chen, *ACS Appl. Mater. Interfaces*, 2014, **6**, 6196–6201.